Preparing for InSight: An Invitation to Participate in a Blind Test for Martian Seismicity

by J. F. Clinton, D. Giardini, P. Lognonné, B. Banerdt, M. van Driel, M. Drilleau, N. Murdoch, M. Panning, R. Garcia, D. Mimoun, M. Golombek, J. Tromp, R. Weber, M. Böse, S. Ceylan, I. Daubar, B. Kenda, A. Khan, L. Perrin, and A. Spiga

ABSTRACT

The InSight (Interior exploration using Seismic Investigations, Geodesy and Heat Transport) lander will deploy a seismic monitoring package on Mars in November 2018. In preparation for the data return, we prepared a blind test in which we invite participants to detect and characterize seismicity included in a synthetic dataset of continuous waveforms from a single station that mimics both the streams of data that will be available from InSight, as well as expected tectonic and impact seismicity and noise conditions on Mars. We expect that the test will ultimately improve and extend the current set of methods that the InSight team plan to use in routine analysis of the Martian dataset.

Electronic Supplement: Candidate 1D models for use in the InSight blind test not shown in the main article.

INTRODUCTION

The National Aeronautics and Space Administration (NASA) Discovery InSight (Interior exploration using Seismic Investigations, Geodesy and Heat Transport) mission (Banerdt *et al.*, 2013) will deploy a lander equipped with geophysical and meteorological sensors on the Martian surface at Elysium Planita (Golombek *et al.*, 2016; Fig. 1). The geophysical station will include two three-component ultrasensitive seismometers (SEIS), a very broadband (VBB) sensor and a short-period sensor (Lognonné *et al.*, 2012; Lognonné and Pike, 2015). The seismic goals of the mission include (1) providing 1D models of Mars' mantle and core to within ±5% uncertainty in seismic wavespeeds as well as the thickness of the crust; and (2) measuring the activity and distribution of seismic events on Mars, including both tectonic and impact seismicity (Banerdt *et al.*, 2013). The InSight launch is targeted for May 2018, landing in November 2018, with nominal operation for 1 Martian year, equivalent to roughly 2 Earth years. InSight will return continuous seismic data at 2 samples per second with the option of retrieving limited data extracts at 20 or 100 samples per second. Raw seismic and atmospheric waveform data will be made openly available within three months of data collection up until mid-2019, afterward with an even shorter delay.

To prepare for the data analysis, a number of ground services are being set up. The French Space Agency Centre National d'Etudes Spatiales will operate SeIS on Mars Operation Center that will manage the SEIS payload and provide raw waveforms in near real time in miniSEED, the standard seismic data exchange format, as well as channel metadata. These data will be archived and distributed by the Mars SEIS Data Service, operated by Institut de Physique du Globe de Paris (IPG Paris) (targeting both scientists and educational collaborators). Data for open release will also be available from NASA Planetary Data System and Incorporated Research Institutions for Seismology (IRIS) Data Management Center. The Marsquake Service (MQS), operated at ETH Zürich, and the Mars Structural Service (MSS), at IPG Paris, will prepare and release seismicity catalogs and Martian structural models, in close collaboration with the Jet Propulsion Laboratory and other SEIS partners.

The main tasks of the MQS are identification and characterization of seismicity and the management of the Martian seismic-event catalog. In advance of the mission, the InSight team developed a series of single-station event-location methods using (a) multiorbit surface waves and (b) differential body- and surface-wave arrival times relying on (initially *a priori*) 1D and 3D structural models (Panning *et al.*, 2015; Böse *et al.*, 2017). MSS and MQS expect to use iterative inversion techniques to revise these structural models and event locations (Khan *et al.*, 2016; Panning *et al.*, 2016).

 doi: 10.1785/0220170094

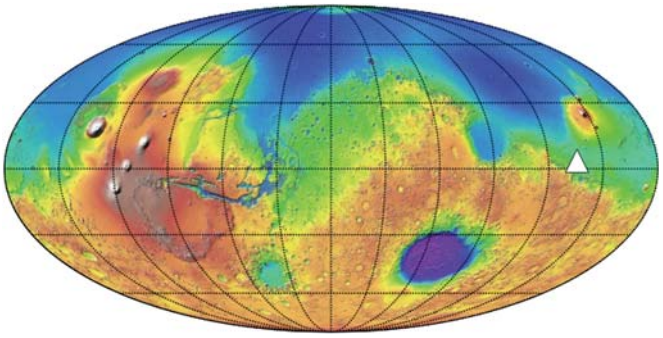

▲ **Figure 1.** Map showing planned location of the InSight lander on Mars (white triangle). Background image is from Mars Orbiter Laser Altimeter (MOLA; Smith *et al.*, 2001).

In an effort to seek methodological advances and test current single-station location approaches, and also to raise awareness and the level of preparation within the scientific community for the data that will arrive from Mars, the InSight SEIS team has designed a blind test in which any interested parties are invited to participate by analyzing synthetic Martian seismograms and providing a Martian seismicity catalog. This test follows those implemented in similar science communities, for example, for the Laser Interferometer Space Antenna Project (Arnaud *et al.*, 2007; Babak *et al.*, 2010). The test will begin on 1 August 2017, with the release of the test dataset and all supplementary material, and will close six months later on 1 February 2018.

Summary of the Test Dataset

The blind test dataset consists of a 12-month period (1 Earth year, roughly half a Martian year) of continuous waveform data that simulates what we can expect to retrieve from InSight. Realistic estimates of background seismic noise are combined with synthetic marsquake seismograms generated using a 1D Mars model using a seismicity catalog that includes about 200 tectonic and 35 impact events. The element of blindness is introduced by use of an unknown Mars model and randomly generated seismicity catalogs.

The 1D structural model is selected from a suite of 14 *a priori* structural models extended from Panning *et al.* (2016), based on structural models from Zharkov and Gudkova (2005), Rivoldini *et al.* (2011), and Khan *et al.* (2016) (see Table 1 and Fig. 2). The synthetic waveforms for the marsquake sources are computed using AxiSEM (Nissen-Meyer *et al.*, 2014) and Instaseis (van Driel *et al.*, 2015).

A catalog of tectonic events is prepared following the method outlined in Ceylan *et al.* (2017). Golombek *et al.* (1992) and Knapmeyer *et al.* (2006) show that the rate of tectonic seismicity on Mars may be similar to continental regions of the Earth, with a total moment release of order 10^{18} N·m per year. We generate synthetic marsquake catalogs that are statistically consistent with this current expectation of Martian seismicity with random time, location, and depth distribution (between 2 and 100 km). Maximum event magnitude is set near M_w 5.0, and no events below M_w 2.5 are included. An example event catalog is shown in Figure 3.

Table 1
Summary of the 14 Candidate 1D Mars Models

Velocity Model Name	Moho Depth (km)	Range of Direct *P*-Wave Shadow Zones (°)	Range of Direct *S*-Wave Shadow Zones (°)	References
DWAK	66	None	20.0–26.5	Khan *et al.* (2016)
EH45ThotCrust2	85	None (105.0)	7.0–57.5 (125.0)	Rivoldini *et al.* (2011)
EH45Tcold	90	None	24.5–28.5	Rivoldini *et al.* (2011)
EH45TcoldCrust1	85	None	10.5–29.5	Rivoldini *et al.* (2011)
EH45TcoldCrust1b	85	None	10.5–29.5	Rivoldini *et al.* (2011)
EH45ThotCrust2b	85	None (106.0)	7.0–57.5 (125.0)	Rivoldini *et al.* (2011)
DWThot	90	None	25.5–65.5	Rivoldini *et al.* (2011)
DWThotCrust1	90	None	11.5–60.0	Rivoldini *et al.* (2011)
DWThotCrust1b	90	None	11.0–61.5	Rivoldini *et al.* (2011)
Gudkova	50	None	None	Zharkov and Gudkova (2005)
LFAK	56	None	20.0–28.0	Khan *et al.* (2016)
MAAK	69	None	None	Khan *et al.* (2016)
SANAK	32	None (105.0)	22.0–50.5 (133.0)	Khan *et al.* (2016)
TAYAK	77	None	None	Khan *et al.* (2016)

No model has an apparent *P*-wave shadow zone. However, three models have significantly shorter maximum distance for direct *P* waves with respect to direct *S* waves. For these models, the maximum direct *P*- and *S*-wave ranges are indicated in parenthesis. References correspond to primary publications describing the generation method. The ranges of key parameters for the models are shown in Figure 2. Detail information for each model is shown in Figures 5 and 6 and in Ⓔ Figures S1–S12, available in the electronic supplement to this article.

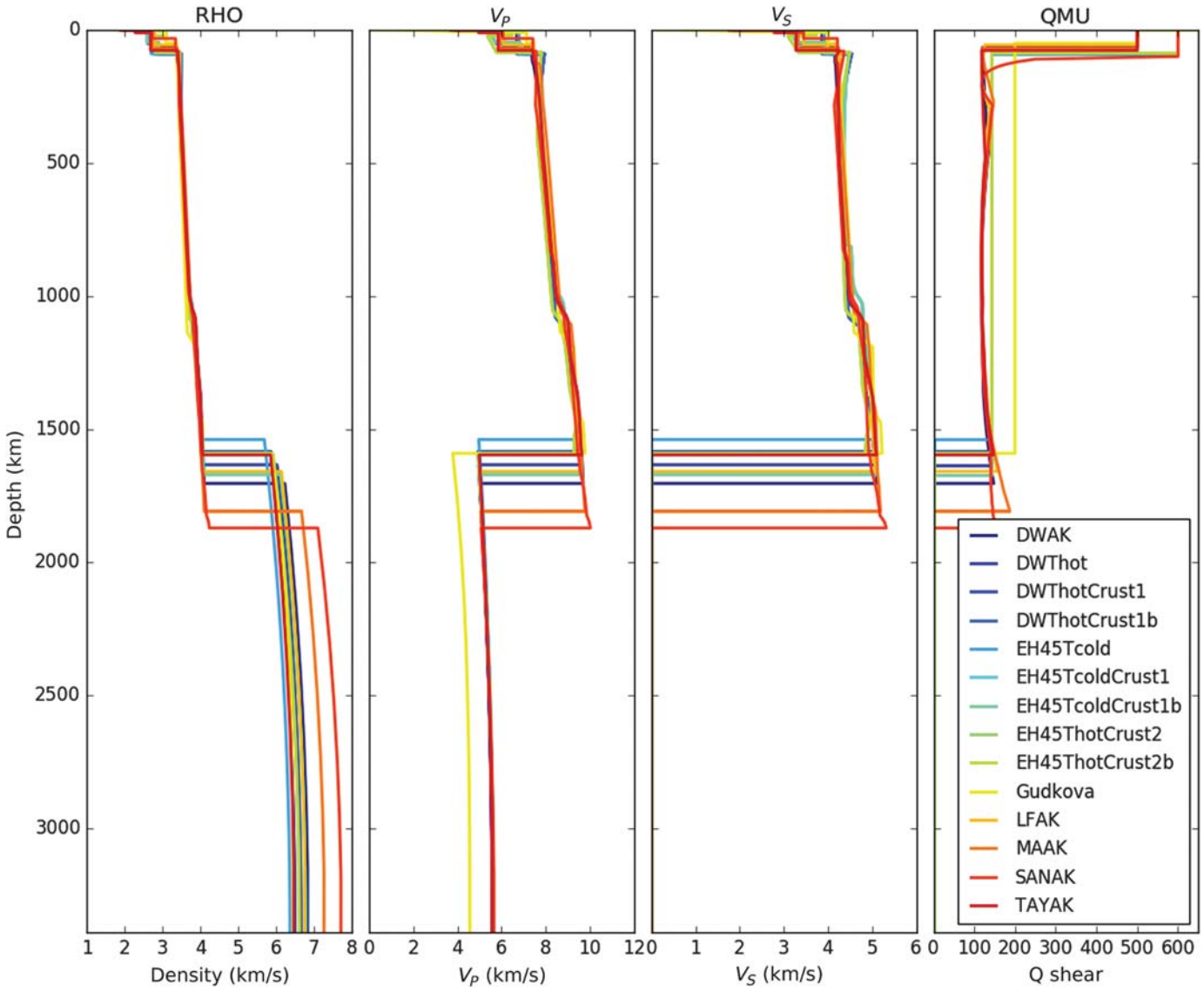

▲ **Figure 2.** Vertical profile showing ranges of seismic velocities, density, and shear attenuation for the 14 candidate velocity models. See Table 1 for additional details on each model.

The impact catalog is derived using a model based on Teanby (2015), based on the distribution of observed newly dated craters (Daubar *et al.*, 2013). Again, a globally random distribution is assumed. To restrict amplitudes to levels similar to M_w 2.5 events, we only include impacts with impactor mass larger than 100 kg.

The continuous time series are created by superimposing the event seismograms onto seismic noise that reflects the current estimate of what may be encountered for the surface installation of the InSight seismometer (Murdoch *et al.*, 2016, 2017; D. Mimoun *et al.*, unpublished manuscript, 2017; see Data and Resources). This signal includes noise generated by the sensors and systems themselves, as well as through the environment (such as fluctuating pressure-induced ground deformation, the magnetic field, and temperature-related noise) and the nearby lander (such as wind-induced solar panel vibrations). The atmospheric variables, with the exception of the magnetic-field variations, are derived from large eddy simulations (LESs; Spiga *et al.*, 2010) at short period and general circulation models (GCMs) at longer periods. This ensures a self-consistent description of the atmospheric dynamics. Also, because the atmospheric data provided are directly correlated with the seismic noise, this offers the possibility of applying decorrelation techniques to the seismic data to reduce the atmospheric noise (e.g., Murdoch *et al.*, 2017). Furthermore, to simulate more-realistic operational conditions, the noise model also includes glitches.

An example of seismograms from sample marsquakes, also including noise, is in Figure 4, derived as detailed in Ceylan *et al.* (2017), using similar but different sets of 1D velocity models and noise.

It is important to note that, although we attempted to generate a dataset representative of the continuous data, the

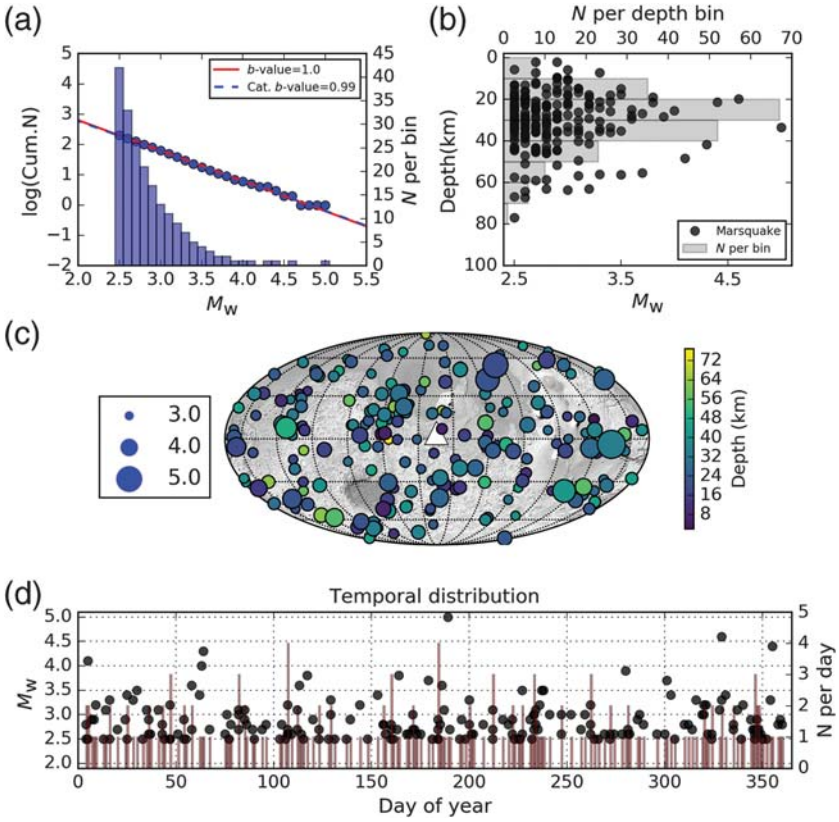

▲ **Figure 3.** One possible realization of the Martian seismicity catalog used in the blind test. (a) Comparison of *b*-values for the catalog (dashed blue line, $b = 0.99$) and the reference catalog (solid red line, $b = 1.0$). Total number of events in each catalog is $N = \sim 200$; in this case $N = 202$. (b) Event depth distribution, following a skewed Gaussian curve. (c) Map showing location of seismicity. The white triangle indicates the location of the seismic station. The background image is from MOLA. (d) Temporal evolution of seismicity. Note that origin times, distance, and back-azimuth values are randomly assigned. There are no constraints on the temporal distribution of events, so they may overlap.

provided waveform data remain ideal and likely optimistic with respect to the future InSight data. Because we use 1D models for the seismic signals, we do not include any effects of 3D structure. Such effects are likely to be important on Mars, because numerical wave propagation through 3D models, including topography and crustal thickness variation, indicates body-wave scattering and surface-wave multipathing that can significantly impact the waveforms (Bozdağ *et al.*, 2017). The near-surface Martian atmosphere is characterized by a strong diurnal cycle, with intense convective turbulence in the day (leading to seismic noise) and, conversely, stable conditions during the night. This diurnal cycle repeats itself on a very regular basis each day, with a second-order modulation by seasonal trends, given InSight's equatorial position. The noise signals for the blind test are repetitions of a daily noise typical of the northern spring equinox (i.e., heliocentric longitude Ls = 0), with environmental wind of 10 m/s, and they do not include microseismic noise (e.g., noncoherent seismic waves generated by the Martian atmospheric activity) or seasonal noise variations (e.g., regional storms and depressions).

Participating in the Blind Test

We invite the wider scientific community to explore the dataset and identify and characterize the seismicity. To contribute to the blind test, any interested persons should provide:

- notification of your intention to contribute to the test, preferably by the end of September 2017 (done by completing a form before gaining access to the waveform catalog), and
- submission of an event catalog by 1 February 2018, with a description of the methods used.

There is no strict format requirement for the event catalog, although our preferred format is QuakeML (Schorlemmer *et al.*, 2011). Any structured ASCII or excel file with instructions for parsing are acceptable. However, catalogs should include the following information:

- (mandatory) event location (distance and azimuth from the InSight lander, or latitude and longitude) and origin time,
- (optional) event depth, magnitude or seismic moment, and phase information,
- (optional) a focal-mechanism solution,
- (optional) event type (tectonic vs. impact),
- (optional) uncertainties for these parameters, and
- (mandatory) a short description of methods used or corresponding references.

The submitted catalogs will be compared in various different ways. There will be no overall ranking but scores assigned in each category. Scoring will be measured separately for three magnitude classes: M_w 4+, M_w 3–4, and M_w 2.5–3. The categories will be:

- Total events in catalog: numbers of correct and false events;
- Discrimination: numbers of correct and false impacts;
- Accuracy: mean and standard deviation of the difference to true value for each of distance, azimuth, depth, and seismic moment; and
- Visual comparison of focal mechanisms with true solutions.

Further, any group that is willing to speculate on the structural model used, or that can identify core phases, can get bonus credit!

To conclude the blind test, we intend to review the performance of all contributors and to summarize the methodologies used by the different groups in an *SRL* article in early 2018. The actual seismicity and impact catalog and model used to generate the blind test data will also be released. All groups who contribute a catalog to the blind test will be invited to be coauthors.

In addition to the information provided in this article, a website for the blind test (see Data and Resources) will include

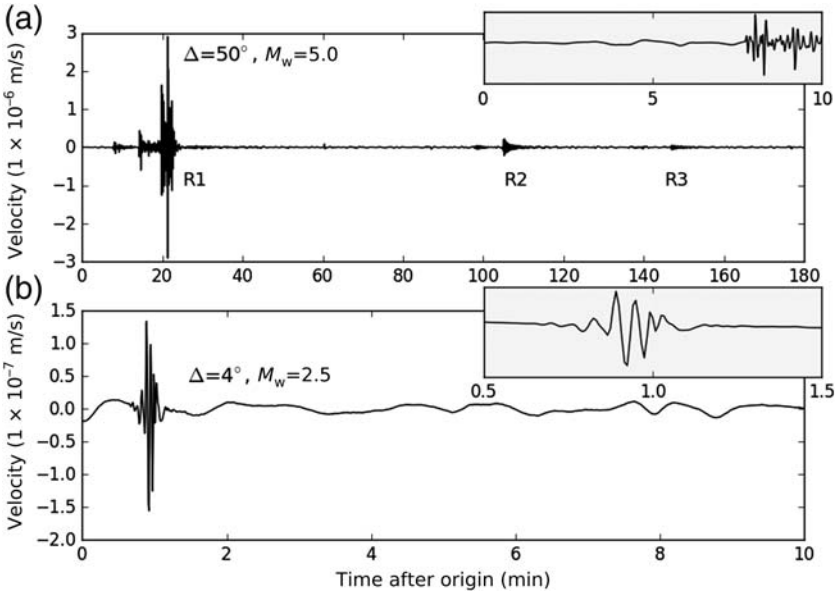

▲ **Figure 4.** Examples of (vertical) synthetic marsquake seismograms for (a) an event at 50° distance with a magnitude of M_w 5.0, and (b) an event at 4°, M_w 2.5. Inset plots highlight the first-arrival body waves. The waveforms include realistic seismic noise. Data are band-pass filtered between 2 and 200 s. R1, R2, and R3 in (a) indicate Rayleigh-wave energy traveling along the minor arc (R1), the major arc (R2), and multiorbit R1 (R3).

information on how to access the waveform data and submit results and will provide related information that may aid interpretation. Comments or requests for clarifications can be sent to the indicated blind-test contact points. All clarifications, updates, and news will be posted openly on this page.

The body of this article includes further detailed material critical to understanding and participating in the blind test. We detail how the structural models are created and highlight features of each model. Then, we describe how the continuous VBB synthetic waveform data are built. This includes the generation of the seismic source catalog, the numerical methods used to generate the event synthetics, and the background seismic noise that reflects what we expect to be recorded by the InSight SEIS instrument. We conclude with information on the resources that are available to test participants.

A PRIORI MODELS

Fourteen 1D structural models for Mars have been selected as candidates for the blind test (Table 1; Fig. 1). Radially symmetric models of seismic *P*- and *S*-wave velocities, shear and bulk attenuation, and density are taken from the studies of Zharkov and Gudkova (2005), Rivoldini *et al.* (2011), and Khan *et al.* (2016), respectively. The models are generally constructed so that the current set of available geodetic data (mean mass and moment of inertia, tidal Love number, and global tidal dissipation) is satisfied. Using either parameterized phase diagram or Gibbs free-energy-minimization approaches, the models are constructed assuming a known bulk mantle composition and thus a mineralogy that derives from geochemical, cosmochemical, and isotopic analyses of Martian rocks and primitive solar-system material (e.g., Taylor, 2013). On this basis, physical properties for the crust, mantle, and core can be computed from equation-of-state modeling (for more detailed information, we refer the interested reader to the original studies). Shear and bulk attenuation models are either scaled from a preliminary reference Earth model (PREM) (Dziewonski and Anderson, 1981) or computed based on a specific viscoelastic model. Specific details for each model are shown in Figures 5 and 6 and Ⓔ Figures S1–S12, available in the electronic supplement to this article, showing (a) seismic *P*- and *S*-wave velocities and density as a function of depth, (b) flat-Earth-transformed seismic-wave velocities (Shearer, 1999) in the crust and upper mantle for the purpose of highlighting regions that can result in travel-time shadow zones, (c) Rayleigh- and Love-wave phase and group velocity dispersion curves, and (d) travel times for a set of seismic body-wave phases: *P*, *PP*, *S*, and *SS* for an event at the surface.

Low-Velocity Zones in the Upper Mantle

Low-velocity zones (LVZs) are present in most of the models and appear both in the crust and upper mantle, as indicated in Table 1. If the decrease in velocity is strong enough so that rays do not turn upward, this leads to shadow zones for body-wave arrivals; that is, these phases cannot be observed for certain distances. This is very important when interpreting first-arriving *P* and *S* waves, which can easily be confused with later-arriving phases such as *PP* and *SS*. The criterion for rays to not turn upward in a spherical model is that the flat-Earth-transformed velocities have a negative gradient. Geometrically, this means that horizontal rays are then bent downward with respect to the arc at that radius. Such regions are highlighted in Figures 5 and 6 and in Ⓔ Figures S1–S12 by gray shading.

MARSQUAKE CATALOG

Tectonic Catalog

The synthetic tectonic event catalog follows Ceylan *et al.* (2017). The catalog comprises about 200 events (the largest is about M_w 5.0), and there is a lower-magnitude cutoff of M_w 2.5. Events are randomly distributed across the planet; we do not apply any constraint on spatial distribution, such as forcing events to cluster along geologic features, and depths are randomly assigned in a skewed Gaussian distribution between 2 and 100 km. Events are also randomly spaced in time. To minimize source-type effects, we use the approach of Tape and Tape (2015) to uniformly distribute double-couple events. No aftershocks are included. Catalog versions can be created

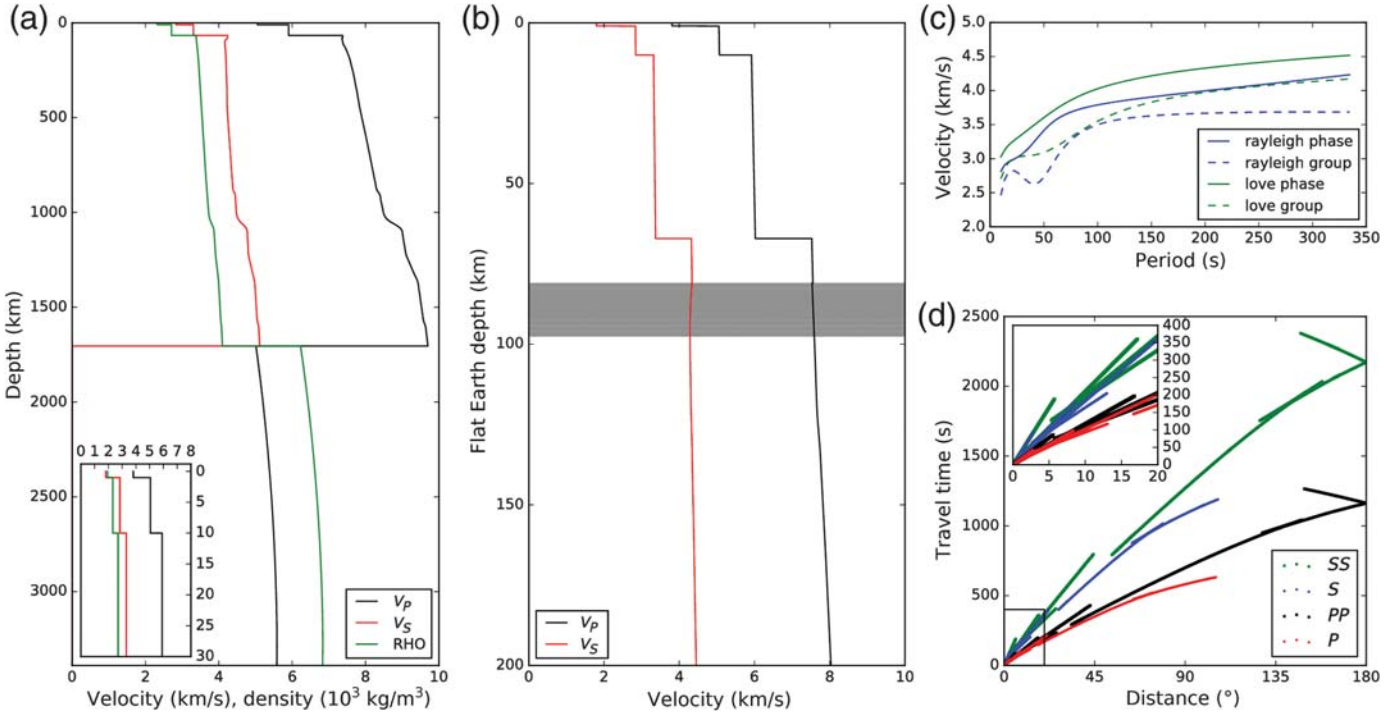

▲ **Figure 5.** Vertical profile of (a) seismic velocities and density, (b) flat-Earth-transformed seismic velocities, (c) dispersion curves, and (d) travel times for model DWAK. Low-velocity zones (LVZ, regions with a negative velocity gradient for either or both *P* and *S*) are indicated in gray in (b). The LVZ may or may not lead to shadow zones for direct-arriving phases shown in (d).

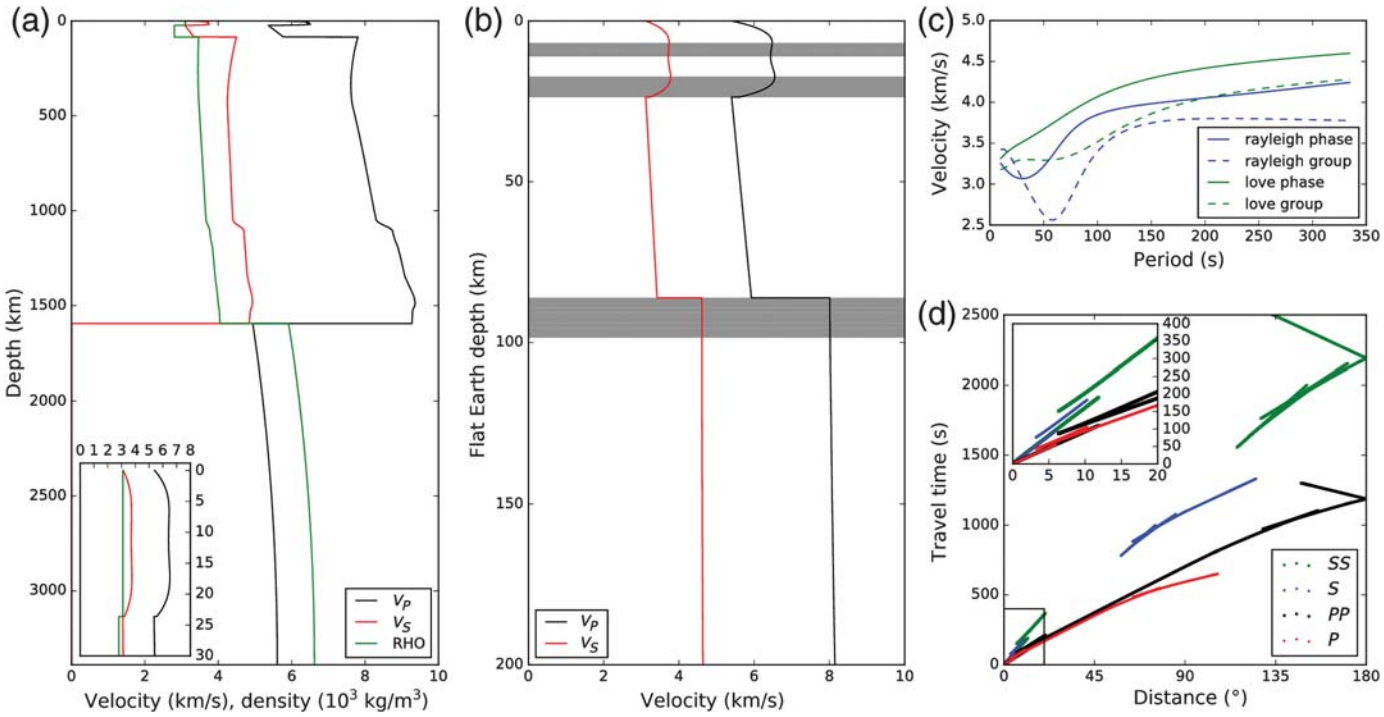

▲ **Figure 6.** Same as Figure 5 but for model EH45ThotCrust2.

on demand with randomized location, depth, and magnitude distributions. One realization of such a catalog is shown in Figure 3.

Impact Catalog

For the impact catalog, we used a model based on Teanby (2015), which uses the distribution of observed newly dated

craters (Daubar *et al.*, 2013), combined with atmospheric fragmentation modeling (Williams *et al.*, 2014) to extrapolate down to smaller-sized impacts on the surface than can be observed from the orbit. Dated current impacts (Daubar *et al.*, 2013) have an observational bias toward dust-covered areas of Mars, but there is no evidence to indicate a strongly nonuniform distribution of impactors. Thus, nonuniform cratering, such as a variation with latitude (Le Feuvre and Wieczorek, 2008), is not included, because the effect is small. We calculate the impactor masses for each diameter using the Holsapple impact calculator, v.2.5, 2017 (see Data and Resources) and the following parameters, which are most appropriate for these sizes on Mars: target material of dry sand (1.7 g/cm^3, no cohesion, 33° friction angle, 30% porosity), Martian gravity (0.376g), impactor material of rock (3 g/cm^3), impact velocity of 10 km/s, and impact angle of 45°. We then varied those masses by choosing a random value from a normal distribution around that calculated mass with 20% standard deviation. The number in each bin is according to the Teanby (2015) model, calculated for the entire surface of Mars over one Earth year. Each distribution includes one impact on the order of 10,000 kg in the largest bin, which would produce a 31–44 m diameter crater. Events are restricted to impactor masses above 100 kg, a size that generates waveform amplitudes similar to an M_w 2.5 tectonic event. About 35 such events are included in the catalog.

Like the tectonic catalog, impact events are then randomly distributed both spatially and temporally. Also randomly assigned are the azimuth of the impactor (the direction from which the impactor is coming), ranging from 0° to 360°, with north = 0°, east = 90°, and the impact angle (degrees from vertical) according to a normal distribution around 45°, with a standard deviation of 10°. The value of 45° is that expected to be most common for bodies approaching from random directions (Shoemaker, 1961), and the standard deviation was chosen to roughly match what is observed for newly dated Martian crater clusters (Daubar *et al.*, 2017). The impact velocity is 10 km/s in all cases, which is approximately the mean expected impact velocity at Mars (JeongAhn and Malhotra, 2015). Impact events are modeled as a single force in a moment-tensor representation following Gudkova *et al.* (2015).

Magnitudes

We ask participants in the blind test to compute M_w or the seismic moment for all identified events. Because of poor signal-to-noise ratio and uncertain locations, it may be preferable to compute single-station magnitudes using a band-passed portion of the seismic waveforms, similar to the traditional magnitude scales used on Earth, such as the local magnitude M_L, body-wave magnitude m_b, and surface-wave magnitude M_s. For the Mars equivalent magnitudes, we append subscript M. We calibrated the following scaling relations for the filtered peak displacement amplitude A measured in meters (taken over all three components Z, N, and E for M_{LM} and m_{bM} and determined as max $\sqrt{(N^2 + E^2)}$ for M_{SM}), epicentral distance Δ in degrees, and source depth z in kilometers (Böse *et al.*, 2017):

- local magnitude, $\Delta \le 10°$

$$M_{LM} = \frac{2}{3}\log_{10}(A) + 1.0\log_{10}(\Delta) + 0.009z + 7.0,$$

- body-wave magnitude, $\Delta \le 110°$

$$m_{bM} = \frac{2}{3}\log_{10}(A) + 0.9\log_{10}(\Delta) + 7.9,$$

- surface-wave magnitude, $\Delta \le 150°$

$$M_{SM} = \frac{2}{3}\log_{10}(A) + 0.8\log_{10}(\Delta) + 7.7$$

Our magnitude definitions differ from the traditional Earth relations to account for the 1-Hz signal cut-off of the synthetic waveforms in this blind test: M_{LM} and m_{bM} are computed at 2 s, using a fourth-order Butterworth band-pass filter with corner frequencies at 0.03 and 0.75 Hz; M_{SM} is computed between 10 and 30 s. The magnitude relations above are calibrated to scale with M_w. Because we are always below the corner frequencies of the events, due to a combination of signal content (the waveforms at this sampling rate are restricted to periods longer than 1 s) and maximum event size ($M_w \sim 5$), the observed scaling of the magnitudes includes the factor of 2/3 to match with the moment magnitude.

These magnitude relations are valid for all seismic-event types in the catalog, both tectonic and impacts events.

M_{LM}, m_{bM}, and M_{SM} have been calibrated using a set of 750 randomly distributed synthetic marsquakes computed for each of 13 1D-structural models as defined in Ceylan *et al.* (2017). These models reflect 1D thin (30 km) and thick (80 km) Martian crust, with varying seismic wavespeeds and densities, combined with two different profiles for temperature and composition for the mantle.

GENERATION OF SYNTHETIC WAVEFORMS FOR EVENTS

We use AxiSEM (Nissen-Meyer *et al.*, 2014) and Instaseis (see Data and Resources; van Driel *et al.*, 2015) to compute Green's function databases on the planetary scale as solutions to the elastic-wave equation, including effects of attenuation.

Numerical simulations are costly even with the axisymmetric scheme of AxiSEM. We compute VBB synthetics that include both the short periods and the duration required by the longest periods expected to be recorded on Mars in a single computation by splicing together seismograms from different simulations to generate a single data stream containing the whole bandwidth of signals. We merge synthetic data from the following sources:

- very short periods targeting body waves (up to 1 s, for a duration of 40 min),
- intermediate periods targeting surface waves (up to 5 s for a duration of 6 hrs), and
- longer periods (up to 20 s, for a duration of 24 hrs).

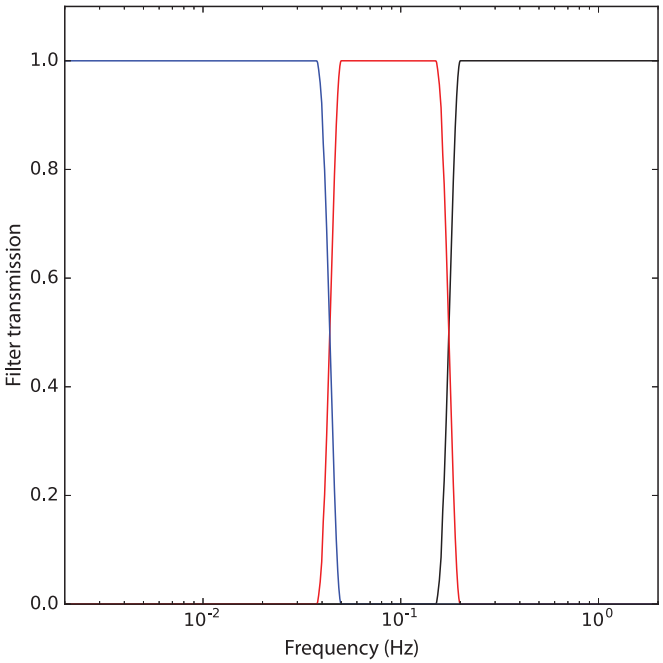

▲ **Figure 7.** Cosine filter applied for merging seismograms.

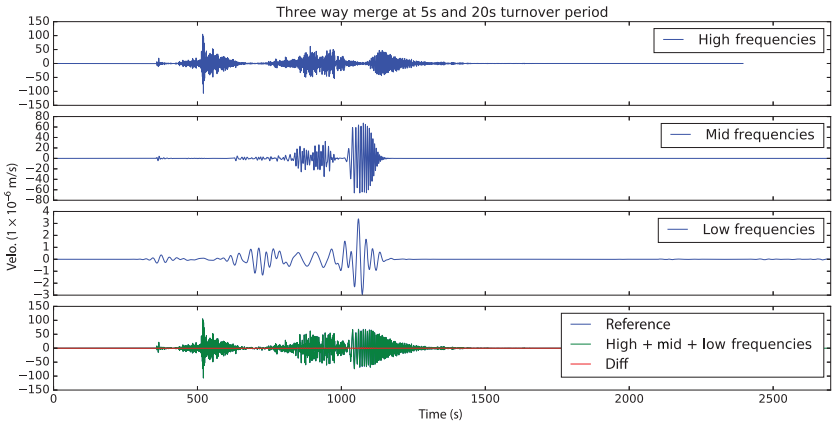

▲ **Figure 8.** Example of seismogram merging. Seismograms are generated for three different durations with different frequency resolution for a teleseismic marsquake using one of the candidate Mars models, as described in the text. In the bottom panel, the three different seismograms are merged following the filter shown in Figure 7, and the sum is compared to the full seismogram ("reference") extracted from the 1 s database. The seismograms include both the (left) *P*- and (middle) surface-wave arrivals.

Merging is accomplished by orthogonal cosine filters, as shown in Figure 7. Figure 8 demonstrates this scheme applied to seismograms generated for a teleseismic event using one of the candidate Mars models, computed as described above, each stored with different sampling rates. Resampling to the 10 Hz sampling used here is done using the Lanczos filters (see figs. 8 and 9 in van Driel *et al.*, 2015). Small differences between the expected and merged seismograms are visible at the resolution limit of the long-period data, but at an amplitude that we deem acceptable for the purpose here.

NOISE

We computed an Earth-year-long time series of realistic Martian environmental and instrumental noise, forming the basis of the continuous waveforms to which the event synthetics are added. A short description of the atmospheric data used, and of the different noise contributions, is provided below. The noise is estimated for the components of the VBB sensor in SEIS.

Mars Atmospheric Simulations

To obtain a reliable description of the atmospheric variability at the InSight landing site, we coupled the results of GCMs, which provide the long-period variations of the meteorological variables, to 3D LESs describing the short-period dynamics of the planetary boundary layers and including the effects of convective cells and vortices (e.g., dust devils). For more details about the GCM and the LES used in this study, see Spiga *et al.* (2010), Millour *et al.* (2015), and Murdoch *et al.* (2017). This approach ensures a self-consistent description of the atmospheric dynamics; however, not all of the complexities of the Martian atmosphere are captured. Specifically, no seasonal variations are taken into account, the background wind velocity and direction imposed to the LES are the same for the whole one-year duration, and no large-scale intense meteorological episodes, such as regional or global dust storm, appear. The LESs have an output every 6 s, and an extrapolation to higher frequency is necessary to provide 1 s signals. Colored noise is thus added to the meteorological parameters in the 0.08–1 Hz band following the local slope of the spectra. We emphasize that this extrapolation results in smaller high-frequency amplitudes than previously assumed (Murdoch *et al.*, 2016; D. Mimoun *et al.*, unpublished manuscript, 2017; see Data and Resources).

Pressure Noise

The seismic noise induced by local pressure fluctuations is computed based on the entire 2D surface pressure field of the LES. A regolith layer overlying fractured bedrock is taken as the subsurface model, and its response to pressure loading is assumed to be elastic and quasi-static. The induced ground deformation is thus calculated, and the corrections for free-air anomaly (minor correction) and for ground tilt (main correction) are taken into account (for more information, see Kenda *et al.*, 2017; Murdoch *et al.*, 2017).

Wind-Induced Mechanical Noise

The dynamic pressure of the wind (provided from the LES data) will produce fluctuating stresses on the Wind and Thermal Shield (WTS) that protects SEIS and on both the nearby lander body and Heat Flow and Physical Properties Probe (HP3). These stresses will subsequently deform the ground,

resulting in a seismic signal that will be registered by SEIS. The proximity of SEIS to the lander, WTS, and HP3 is such that no propagation effects are significant and that the noise is mostly static loading. Full details of the calculations are provided in Murdoch *et al.* (2016).

Thermal and Thermoelastic Noise

The SEIS seismometers are sensitive to the temperature fluctuations; this creates a thermal noise along each of the sensitivity axes. Additionally, if there is an inhomogeneous temperature distribution or an inhomogeneous thermal expansion coefficient, the SEIS vacuum enclosure, the levelling system (LVL), and the ground itself may experience some inhomogeneous thermoelastic expansion or contraction. This will result in a tilt, detected as noise on the horizontal axes of SEIS. The external temperature variations are estimated from the LES (short-period) and GCM (long-period) data. These temperature fluctuations are attenuated by the WTS and, for the VBB components, also by the SEIS vacuum enclosure (these are both modeled as a simple first-order thermal filter with time constants of 5 hrs 30 min and 2 hrs, respectively). As in D. Mimoun, *et al.* (unpublished manuscript, 2017; see Data and Resources), the thermal noise is then calculated, assuming a sensitivity of each VBB component (along its sensitivity axis) of 1.5×10^{-5} m/s^2 K, and the thermoelastic noise calculations assume a tilt sensitivity of SEIS of 5.6×10^{-5}°/K (9.4×10^{-7} rad/K). The lower frequency ($f < 0.15$ mHz) part of the SEIS signal has been calculated with a thermal model of the instrument and ground (326 and 600 nodes, respectively), accounting for diurnal air and ground temperature variations and shadowing effects. The electrical tether connecting SEIS to the lander will also experience some expansion and contraction due to temperature fluctuations, resulting in a tilt of the LVL. However, the assumed tether tilt sensitivity of 1×10^{-11} rad/K makes this contribution negligible.

Magnetic Noise

The magnetic field at the surface of Mars is largely unknown. In the absence of a planetary dynamo, and given the weak crustal magnetization at the Insight landing site (Morschhauser *et al.*, 2014), we assume that the magnetic-field variations are driven by the solar wind. As a proxy for the Martian magnetic-field variations, we use terrestrial equatorial data from the magnetic observatory in Kourou. However, we filter the terrestrial data (high-pass filter over 5 hrs) because the diurnal frequencies are linked to magnetospheric structure that differs between Earth and Mars. The magnetic noise is then calculated (as in D. Mimoun *et al.*, unpublished manuscript, 2017; see Data and Resources), assuming a magnetic sensitivity of each VBB component of 5.4×10^{-10} m/s^2 nT. The noise generated by the magnetometer is accounted for in the magnetic-field data provided as part of the blind test.

Electric-Field Noise

When grain transport occurs on Mars, an electric field is generated at the planet's surface via triboelectric charging of the lofted particles. Because the electrical tether linking SEIS to the lander is sensitive to electric fields, this creates an electric-field noise that will be detected by SEIS. Using the wind shear velocity (LES data), the induced saltation mass flux and resulting electric field are derived following Kok and Renno (2009) and Kok (2010). This electric-field noise is equivalent to an additional voltage noise at the integrator level.

Instrument Noise

The VBB instrument noise incorporated into the data is derived from test results for both the feedback electronics and sensor heads. At long period, most of the noise is associated with the integrator noise of the velocity output of the VBBs, whereas at short period the noise is mostly related to the displacement transducer. Between 0.05 and 1 Hz, the instrument noise is related to the proof mass Brownian noise.

DATA PROVIDED TO PARTICIPANTS

Access to the continuous test waveforms will be provided at the InSight blind test website from 1 August 2017 (see Data and Resources). The dataset made available for the blind test is deliberately made similar to what can be expected from InSight, with some simplifications. In addition to the seismic data, the dataset will include pressure, temperature, magnetic field, and wind speed and direction signals that are correlated with the seismic noise. All waveform data are provided in miniSEED format, at sampling rates consistent with the continuous data return expected during the mission. To encourage participation and accelerate analysis, we additionally provide travel-time tables for a set of seismic phases for all 14 candidate models, as will be used by MQS in the test. The sections below give a short summary of the data that we distribute in support of the blind test. Detailed information for each item can be found at the InSight blind-test website (see Data and Resources).

Time-Series Data

A summary of the available continuous data streams is shown in Table 2. In addition to the three components of basic seismic data, auxiliary atmospheric data that are correlated with the seismic noise are included, which may be useful to take into account for event detection and interpretation. For simplicity, seismic waveforms are presented as ground motion as recorded from a typical broadband seismometer (Streckeisen STS-2) using a 26-bit datalogger and so are provided in counts (cts). A full instrument deconvolution for the seismometer velocity data can be done using the metadata provided (datalessSEED or stationXML), though within the passband between the Nyquist at 1 Hz and 120 s, the data can be converted to velocity (m/s) using the conversion factor of 2.516582×10^9 m/s/cts.

All auxiliary data related to the noise signals (pressure, wind speed and direction, magnetometer, temperature) are provided directly in physical units. Naming conventions follow SEED standards as closely as possible, though location codes are defined internally by the project and reflect the complexity of possible modes of operation. We arbitrarily select the year of

Table 2
Summary of Time-Series Information Made Available for the Blind Test

Data Type	Sampling Rate	Channel Code	Location Code	Units of miniSEED Data
Seismic velocity	2	MH [UVW]	02	Counts
Pressure	2	MDO	02	Pascals
Magnetometer	0.2	VF[123]	02	Tesla
Wind speed	0.1	VWS	13	Meters per second
Wind direction	0.1	VWD	13	Degrees
Temperature	0.1	VKI	03	Degrees Kelvin

the blind test to be 2019. The network code for all synthetic datasets being created in advance of InSight is 7J, and the station code for this test is SYNT2. For the science data from the mission, the network and station codes will be XB and ELYS, respectively.

Station Information

Station information can be extracted in various formats using the International Federation of Digital Seismograph Networks (FDSN) webservice fdsn-station as described in the InSight blind test website (see Data and Resources). In our simulations, the station is located at 4.5° N and 136.0° E, in the western Elysium Planitia region of Mars (Fig. 1).

Western Elysium Planitia lies just north of the global dichotomy boundary between elevated heavily cratered southern highlands and lower standing, less cratered, northern plains. The formation of the northern lowlands is the oldest geological event recognized on Mars occurring in the pre-Noachian (Frey, 2006). The plains of western Elysium Planitia, on which the InSight landing ellipse is located (Golombek *et al.*, 2016), are younger Hesperian (3.7–3.0 Ga) lava flows located between Noachian highlands (> 3.7 Ga) to the south and west, Amazonian (< 3 Ga) lavas from Elysium Mons to the north (Tanaka *et al.*, 2014), and very young lavas (several Ma) from Cerberus Fossae and Athabasca Valles to the east (Vaucher *et al.*, 2009).

Geological mapping and analysis of rocky ejecta craters (Golombek *et al.*, 2016) indicate that the basalts are around 200 m thick and are deposited on older sediments that filled the northern plains after the dichotomy formed. Impact and eolian processes created a fragmented regolith 3–17 m thick on top of the basalts. Moderately low thermal inertia and measurement of rocks in high-resolution images show the regolith has few rocks and is composed of dominantly cohesionless sand or very weakly cemented soils (Golombek *et al.*, 2016). A nearby exposed escarpment shows the fine-grained regolith, which grades into coarse, blocky ejecta with 1-m to 10-m scale boulders that overlies strong, jointed bedrock (Warner *et al.*, 2017). The grading of finer grained regolith into coarser, blocky ejecta is exactly what would be expected for a surface impacted by craters with a steeply dipping negative power-law distribution in which smaller impacts vastly outnumber larger impacts that would excavate more deeply beneath the surface (e.g., Shoemaker and Morris, 1969; Hartmann *et al.*, 2001). Knapmeyer *et al.* (2016) used this stratigraphy, along with laboratory measurements (Delage *et al.*, 2017), to develop a model of elastic properties with a stepwise increase in seismic velocity and seismic attenuation Q.

The location of the InSight landing site near the boundary between the highlands and lowlands suggests varying crustal structure to the north versus the south. Estimates of crustal thickness from Mars Orbiter Laser Altimeter (MOLA) topography and gravity from Mars Global Surveyor tracking indicate that the crustal thickness is much thinner in the lowlands (~30 km) compared with the highlands (~60 km) (Neumann *et al.*, 2004).

1D Model Information

For each of the 14 candidate structural models, summary information is provided in Table 1, in Figures 5 and 6, and in Ⓔ Figures S1–S12. The actual velocity models are made available for download at the InSight blind-test website (see Data and Resources) in a variety of standard formats (deck, axisem, nd).

Further, travel-time tables are provided via FTP at the InSight blind-test website (see Data and Resources). We use the TauP Toolkit (Crotwell *et al.*, 1999) to compute travel times for a set of seismic body-wave phases, considering different distance and depth values. To handle triplications, TauP Toolkit reports multiple phase arrivals at a given distance. Surface-wave travel times are computed using the same tool that has been extended to include group velocity dispersion for fundamental-mode Rayleigh and Love waves, as well as higher modes (up to third higher mode) for 21 center frequencies. The travel-time filenames are constructed using the phase name and frequency, where available. Detailed information on the file naming convention is provided at the InSight blind-test website (see Data and Resources), with some examples. These are the same tables that the MQS will use in their effort to locate seismicity in the blind test.

DATA AND RESOURCES

The information on accessing the waveforms, station metadata, other resources such as travel-time tables, and any news on the test updates can be found at http://blindtest.mars.ethz.ch (last accessed July 2017). Figures are created using ObsPy (Krischer *et al.*, 2015) and Generic Mapping Tools (GMT; Wessel *et al.*, 2013). The Mars Orbiter Laser Altimeter (MOLA) dataset is described in Smith *et al.* (2001). The information on the Holsapple impact calculator, v.2.5, 2017, is available at http://keith.aa.washington.edu/craterdata/scaling/index.htm (last accessed May 2017). The other data on AxiSEM and Instaseis are available at www.axisem.info and www.instaseis.net (both last accessed June 2017), respectively. Finally, the details of

the two Earth databases provided by Incorporated Research Institutions for Seismology (IRIS) syngine can be found at www.ds.iris.edu/ds/products/syngine (last accessed April 2017). The unpublished manuscript by D. Mimoun, N. Murdoch, P. Lognonné, K. Hurst, T. Pike, and W. B. Banerdt (2017). "The Mars seismic noise model of the InSight mission", submitted to *Space Sci. Rev.*.

ACKNOWLEDGMENTS

This work was jointly funded by (1) Swiss National Science Foundation and French Agence Nationale de la Recherche (SNF-ANR project 157133 "Seismology on Mars") and (2) Swiss State Secretariat for Education, Research and Innovation (SEFRI project "MarsQuake Service—Preparatory Phase"). Additional support came from the Swiss National Supercomputing Centre (CSCS) under project ID s682. Some of the research described in this article was supported by the InSight (Interior exploration using Seismic Investigations, Geodesy and Heat Transport) project, Jet Propulsion Laboratory, California Institute of Technology, under a contract with the National Aeronautics and Space Administration. This article is InSight Contribution Number 36. The authors would like to thank Laurentiu Danciu for discussions on catalog generation. We are grateful for the careful reviews of the article by two anonymous reviewers and the *SRL* Editor-in-Chief, Zhigang Peng.

REFERENCES

Arnaud, K. A., G. Auger, S. Babak, J. G. Baker, M. J. Benacquista, E. Bloomer, D. A. Brown, J. B. Camp, J. K. Cannizzo, N. Christensen, *et al.* (2007). Report on the first round of the Mock LISA Data Challenges, *Class. Quantum Gravity* **24,** S529, doi: 10.1088/0264-9381/24/19/S16.

Babak, S., J. G. Baker, M. J. Benacquista, N. J. Cornish, S. L. Larson, I. Mandel, S. T. McWilliams, T. Petiteau, E. K. Porter, E. L. Robinson, *et al.* (2010). The Mock LISA Data Challenges: From challenge 3 to challenge 4, *Class. Quantum Gravity* **27,** 084009, doi: 10.1088/0264-9381/27/8/084009.

Banerdt, W. B., S. Smrekar, P. Lognonné, T. Spohn, S. W. Asmar, D. Banfield, L. Boschi, U. Christensen, V. Dehant, W. Folkner, *et al.* (2013). InSight: A discovery mission to explore the interior of Mars, *44th Lunar and Planetary Science Conference*, Lunar and Planetary Inst., Houston, Texas, Abstract Number 1915.

Böse, M., J. Clinton, S. Ceylan, F. Euchner, M. van Driel, A. Khan, D. Giardini, P. Lognonné, and W. B. Banerdt (2017). A probabilistic framework for single-station location of seismicity on Earth and Mars, *Phys. Earth Planet. In.* **262,** 48–65, doi: 10.1016/j.pepi.2016.11.003.

Bozdağ, E., Y. Ruan, N. Metthez, A. Khan, K. Leng, M. van Driel, M. Wieczorek, A. Rivoldini, C. S. Larmat, D. Giardini, *et al.* (2017). Simulations of seismic wave propagation on Mars, *Space Sci. Rev.* 1–24, doi: 10.1007/s11214-017-0350-z.

Ceylan, S., M. van Driel, F. Euchner, A. Khan, J. Clinton, L. Krischer, M. Böse, S. Stähler, and D. Giardini (2017). From initial models of seismicity, structure and noise to synthetic seismograms for Mars, *Space Sci. Rev.*, doi: 10.1007/s11214-017-0380-6.

Crotwell, H. P., T. J. Owens, and J. Ritsema (1999). The TauP Toolkit: Flexible seismic travel-time and ray-path utilities, *Seismol. Res. Lett.* **70,** 154–160, doi: 10.1785/gssrl.70.2.154.

Daubar, I. J., M. E. Banks, N. C. Schmerr, M. P. Golombek, W. K. Hartmann, E. C. S. Joseph, K. Miljković, O. P. Popova, and N. A. Teanby (2017). Crater clusters on Mars: Implications for atmospheric fragmentation, impactor properties, and seismic detectability, *48th Lunar and Planetary Science Conference*, Lunar and Planetary Inst., Houston, Texas, Abstract Number 2544.

Daubar, I. J., A. S. McEwen, S. Byrne, M. R. Kennedy, and B. Ivanov (2013). The current martian cratering rate, *Icarus* **225,** 506–516, doi: 10.1016/j.icarus.2013.04.009.

Delage, P., F. Karakostas, A. Dhemaied, M. Belmokhtar, P. Lognonné, M. Golombek, E. De Laure, K. Hurst, J.-C. Dupla, S. Kedar, *et al.* (2017). An investigation of the mechanical properties of some Martian regolith simulants with respect to the surface properties at the InSight mission landing site, *Space Sci. Rev.* 1–23, doi: 10.1007/s11214-017-0339-7.

Dziewonski, A., and D. L. Anderson (1981). Preliminary reference Earth model, *Phys. Earth Planet. In.* **25,** no. 4, 297–356, doi: 10.1016/0031-9201(81)90046-7.

Frey, H. V. (2006). Impact constraints on, and a chronology for, major events in early Mars history, *J. Geophys. Res.* **111,** no. E08S91, doi: 10.1029/2005JE002449.

Golombek, M., W. Banerdt, K. Tanaka, and D. Tralli (1992). A prediction of Mars seismicity from surface faulting, *Science* **258,** 979–981, doi: 10.1126/science.258.5084.979.

Golombek, M., D. Kipp, N. Warner, I. J. Daubar, R. Fergason, R. L. Kirk, R. Beyer, A. Huertas, S. Piqueux, N. E. Putzig, *et al.* (2016). Selection of the InSight landing site, *Space Sci. Rev.* 1–91, doi: 10.1007/s11214-016-0321-9.

Gudkova, T., P. Lognonné, K. Miljković, and J. Gagnepain-Beyneix (2015). Impact cutoff frequency—momentum scaling law inverted from Apollo seismic data, *Earth Planet. Sci. Lett.* **427,** 57–65, doi: 10.1016/j.epsl.2015.06.037.

Hartmann, W. K., J. Anguita, M. de la Casa, D. Berman, and E. V. Ryan (2001). Martian cratering 7: The role of impact gardening, *Icarus* **149,** 37–53, doi: 10.1006/icar.2000.6532.

JeongAhn, Y., and R. Malhotra (2015). The current impact flux on Mars and its seasonal variation, *Icarus* **262,** 140–153, doi: 10.1016/j.icarus.2015.08.032.

Kenda, B., P. Lognonné, T. Kawamura, A. Spiga, S. Kedar, B. Banerdt, R. Lorenz, D. Banfield, and M. Golombek (2017). Modeling of ground deformation and shallow surface waves generated by Martian dust devils and perspectives for near-surface structure inversion, *Space Sci. Rev.* 1–24, doi: 10.1007/s11214-017-0378-0.

Khan, A., M. van Driel, M. Böse, D. Giardini, S. Ceylan, J. Yan, J. Clinton, F. Euchner, P. Lognonné, N. Murdoch, *et al.* (2016). Single-station and single-event marsquake location and inversion for structure using synthetic Martian waveforms, *Phys. Earth Planet. In.* **258,** 28–42, doi: 10.1016/j.pepi.2016.05.017.

Knapmeyer, M., J. Oberst, E. Hauber, E. Wählisch, C. Deuchler, and R. Wagner (2006). Working models for spatial distribution and level of Mars' seismicity, *J. Geophys. Res.* **111,** no. E11, doi: 10.1029/2006JE002708.

Knapmeyer-Endrun, B., M. P. Golombek, and M. Ohrnberger (2016). Rayleigh wave ellipticity modeling and inversion for shallow structure at the proposed InSight landing site in Elysium Planitia, Mars, *Space Sci. Rev.* 1–44, doi: 10.1007/s11214-016-0300-1.

Kok, J. F. (2010). An improved parameterization of wind-blown sand on Mars that includes the effect of hysteresis, *Geophys. Res. Lett.* **37,** L12202, doi: 10.1029/2010GL043646.

Kok, J. F., and N. O. Renno (2009). Electrification of wind-blown sand on Mars and its implications for atmospheric chemistry, *Geophys. Res. Lett.* **36,** L05202, doi: 10.1029/2008GL036691.

Krischer, L., T. Megies, R. Barsch, M. Beyreuther, T. Lecocq, C. Caudron, and J. Wassermann (2015). ObsPy: A bridge for seismology into the scientific Python ecosystem, *Comput. Sci. Discov.* **8,** 014003, doi: 10.1088/1749-4699/8/1/014003.

Le Feuvre, M., and M. A. Wieczorek (2008). Nonuniform cratering of the terrestrial planets, *Icarus* **197,** 291–306, doi: 10.1016/j.icarus.2008.04.011.

Lognonné, P., and W. T. Pike (2015). Planetary seismometry, in *Extraterrestrial Seismology*, V. Tong and R. Garcia (Editors), Cambridge University Press, Cambridge, United Kingdom, 36–48.

Lognonné, P., B. W. Banerdt, D. Giardini, U. Christensen, D. Mimoun, S. de Raucourt, A. Spiga, R. Garcia, A. Mocquet, M. Panning, *et al.* (2012). Insight and single-station broadband seismology: From signal and noise to interior structure determination, *43rd Lunar and Planetary Science Conference*, Lunar and Planetary Inst., Houston, Texas, Abstract Number 1983.

Millour, E., F. Forget, A. Spiga, T. Navarro, J.-B. Madeleine, L. Montabone, A. Pottier, F. Lefevre, F. Montmessin, J.-Y. Chaufray, *et al.* (2015). The Mars Climate Database (MCD version 5.2), *European Planetary Science Congress 2015*, Nantes, France, 27 September–2 October.

Morschhauser, A., V. Lesur, and M. Grott (2014). A spherical harmonic model of the lithospheric magnetic field of Mars, *J. Geophys. Res.* **119,** no. 6, 1162–1188, doi: 10.1002/2013JE004555.

Murdoch, N., B. Kenda, T. Kawamura, A. Spiga, P. Lognonné, D. Mimoun, and W. B. Banerdt (2017). Estimations of the seismic pressure noise on Mars determined from Large Eddy Simulations and demonstration of pressure decorrelation techniques for the InSight mission, *Space Sci. Rev.* 1–27, doi: 10.1007/s11214-017-0343-y.

Murdoch, N., D. Mimoun, R. F. Garcia, W. Rapin, T. Kawamura, P. Lognonné, D. Banfield, and W. B. Banerdt (2016). Evaluating the wind-induced mechanical noise on the InSight seismometers, *Space Sci. Rev.* 1–27, doi: 10.1007/s11214-016-0311-y.

Neumann, G. A., M. T. Zuber, M. A. Wieczorek, P. J. McGovern, F. G. Lemoine, and D. E. Smith (2004). Crustal structure of Mars from gravity and topography, *J. Geophys. Res.* **109,** no. E08002, doi: 10.1029/2004JE002262.

Nissen-Meyer, T., M. van Driel, S. C. Stähler, K. Hosseini, S. Hempel, L. Auer, A. Colombi, and A. Fournier (2014). AxiSEM: Broadband 3-D seismic wavefields in axisymmetric media, *Solid Earth* **5,** 425–445, doi: 10.5194/se-5-425-2014.

Panning, M. P., E. Beucler, M. Drilleau, A. Moquet, P. Lognonné, and W. B. Banerdt (2015). Verifying single-station seismic approaches using Earth-based data: Preparation for data return from the InSight mission to Mars, *Icarus* **248,** 230–242, doi: 10.1016/j.icarus.2014.10.035.

Panning, M. P., P. Lognonné, W. B. Banerdt, R. Garcia, M. Golombek, S. Kedar, B. Knapmeyer-Endrun, A. Mocquet, N. A. Teanby, J. Tromp, *et al.* (2016). Planned products of the Mars structure service for the InSight mission to Mars, *Space Sci. Rev.* 1–40, doi: 10.1007/s11214-016-0317-5.

Rivoldini, A., T. Van Hoolst, O. Verhoeven, A. Mocquet, and V. Dehant (2011). Geodesy constraints on the interior structure and composition of Mars, *Icarus* **213,** no. 2, 451–472, doi: 10.1016/j.icarus.2011.03.024.

Schorlemmer, D., F. Euchner, P. Kästli, and J. Saul (2011). QuakeML: Status of the XML-based seismological data exchange format, *Ann. Geophys.* **54,** no. 1, 59–65, doi: 10.4401/ag-4874.

Shearer, P. M. (1999). *Introduction to Seismology*, Cambridge University Press, Cambridge, United Kingdom, 260 pp.

Shoemaker, E. M. (1961). Interpretation of lunar craters, in *Physics and Astronomy of the Moon*, Z. Kopal (Editor), Academic Press Inc., London, United Kingdom, 283–359, doi: 10.1016/B978-1-4832-3240-9.50012-2.

Shoemaker, E. M., and E. C. Morris (1969). Thickness of the regolith, in *Surveyor: Program Results*, NASA Special Paper Number 184, U.S. Government Printing Office, Washington, D.C., 96–98.

Smith, D. E., M. T. Zuber, H. V. Frey, J. B. Garvin, J. W. Head, D. O. Muhleman, G. H. Pettengill, R. J. Phillips, S. C. Solomon, H. J. Zwally, *et al.* (2001). Mars Orbiter laser altimeter: Experiment summary after the first year of global mapping of Mars, *J. Geophys. Res.* **106,** 23,689–23,722.

Spiga, A., F. Forget, S. R. Lewis, and D. P. Hinson (2010). Structure and dynamics of the convective boundary layer on Mars as inferred from large-eddy simulations and remote-sensing measurements, *Q. J. Roy. Meteorol. Soc.* **136,** 414–428, doi: 10.1002/qj.563.

Tanaka, K. L., J. A. Skinner Jr., J. M. Dohm, R. P. Irwin III, E. J. Kolb, C. M. Fortezzo, T. Platz, G. G. Michael, and T. M. Hare (2014). *Geologic Map of Mars*, U.S. Geol. Surv. Scientif. Investig. Map 3292, scale 1:20,000,000, pamphlet 43 pp., doi: 10.3133/sim3292.

Tape, W., and C. Tape (2015). A uniform parametrization of moment tensors, *Geophys. J. Int.* **202,** 2074–2081. doi: 10.1093/gji/ggv262.

Taylor, G. J. (2013). The bulk composition of Mars, *Chem. Erde Geochem.* **73,** no. 4, 401–420.

Teanby, N. A. (2015). Predicted detection rates of regional-scale meteorite impacts on Mars with the InSight short-period seismometer, *Icarus* **256,** 49–62, doi: 10.1016/j.icarus.2015.04.012.

van Driel, M., L. Krischer, S. C. Stähler, K. Hosseini, and T. Nissen-Meyer (2015). Instaseis: Instant global seismograms based on a broadband waveform database, *Solid Earth* **6,** 701–717, doi: 10.5194/se-6-701-2015.

Vaucher, J., D. Baratoux, N. Mangold, P. Pinet, K. Kurita, and M. Grégoire (2009). The volcanic history of central Elysium Planitia: Implications for martian magmatism, *Icarus* **204,** no. 2, 418–442, doi: 10.1016/j.icarus.2009.06.032

Warner, N. H., M. P. Golombek, J. Sweeney, R. Fergason, R. Kirk, and C. Schwartz (2017). Near surface stratigraphy and regolith production in southwestern Elysium Planitia, Mars: Implications for Hesperian-Amazonian terrains and the InSight lander mission, *Space Sci. Rev.* 1–44, doi: 10.1007/s11214-017-0352-x.

Wessel, P., W. H. F. Smith, R. Scharroo, J. F. Luis, and F. Wobbe (2013). Generic mapping tools: Improved version released, *Eos Trans. AGU* **94,** 409–410.

Williams, J.-P., A. V. Pathare, and O. Aharonson (2014). The production of small primary craters on Mars and the Moon, *Icarus* **235,** 23–36, doi: 10.1016/j.icarus.2014.03.011.

Zharkov, V. N., and T. V. Gudkova (2005). Construction of Martian interior model, *Sol. Syst. Res.* **39,** no. 5, 343–373.

J. F. Clinton
M. Böse[1]
Swiss Seismological Service, ETH Zürich
Sonneggstrasse 5, 8092
Zurich, Switzerland
jclinton@sed.ethz.ch

D. Giardini
M. van Driel
S. Ceylan
A. Khan
Institute of Geophysics, ETH Zürich
Sonneggstrasse 5, 8092
Zurich, Switzerland

P. Lognonné
M. Drilleau
B. Kenda
Institut de Physique du Globe de Paris
Sorbonne Paris Cité, Université Paris Diderot
75013 Paris, France

B. Banerdt
M. Golombek
I. Daubar
Jet Propulsion Laboratory

California Institute of Technology
Pasadena, California 91109 U.S.A.

N. Murdoch
R. Garcia
D. Mimoun
ISAE-SUPAERO
Université de Toulouse
DEOS/Systémes Spatiaux
31055 Toulouse, Cedex 4
France

M. Panning
Department of Geological Sciences
University of Florida
Gainesville, Florida 32611 U.S.A.

J. Tromp
Department of Geosciences
Princeton University
Princeton, New Jersey 08544 U.S.A.

R. Weber
NASA Marshall Space Flight Center
ST13/NSSTC 2047
Huntsville, Alabama 35805 U.S.A.

L. Perrin
Centre National d'Etudes Spatiales
18 Avenue Edouard Belin
31400 Toulouse, France

A. Spiga
Laboratoire de Météorologie Dynamique
UMR CNRS 8539
Institut Pierre-Simon Laplace
Sorbonne Universités
75252 Paris, France

Published Online 12 July 2017

[1] Also at Institute of Geophysics, ETH Zürich, Sonneggstrasse 5, 8092, Zurich, Switzerland.